

Geophysical Research Letters



RESEARCH LETTER

10.1029/2020GL092238

Key Points:

- A novel technique, distributed temperature sensing (DTS) below a tethered balloon, reveals unknown details of the morning transition
- The morning transition, despite its strong spatiotemporal variability, is robustly determined by changes in static stability
- DTS provides first evidence that the transition occurs simultaneously at the stable boundary bottom and top, and is subject to advection and counter-gradient flux

Supporting Information:

Supporting Information may be found in the online version of this article.

Correspondence to:

C. K. Thomas,
christoph.thomas@uni-bayreuth.de

Citation:

Fritz, A. M., Lapo, K., Freundorfer, A., Linhardt, T., & Thomas, C. K. (2021). Revealing the morning transition in the mountain boundary layer using fiber-optic distributed temperature sensing. *Geophysical Research Letters*, *48*, e2020GL092238. <https://doi.org/10.1029/2020GL092238>

Received 21 DEC 2020

Accepted 13 APR 2021

Revealing the Morning Transition in the Mountain Boundary Layer Using Fiber-Optic Distributed Temperature Sensing

A. M. Fritz¹ , K. Lapo^{1,2} , A. Freundorfer¹ , T. Linhardt¹ , and C. K. Thomas^{1,2} 

¹Micrometeorology Group, University of Bayreuth, Bayreuth, Germany, ²Bayreuth Center of Ecology and Environmental Research (BayCEER), University of Bayreuth, Bayreuth, Germany

Abstract In the morning, the nocturnal stable boundary layer, SBL, transitions into its daytime convective counterpart substantially impacting the distribution of temperature, humidity, and pollutants. Applying distributed temperature sensing (DTS) below a tethered balloon (2–200 m) and along a tower (0–11 m), for the first time we observed three morning transitions (MTs) in a mountain boundary layer with high temporal (<10 s) and spatial (<0.25 m) resolutions. We show that MTs are best derived from a change in static stability from synchronous DTS observations. Our findings confirm that the MT occurs at the SBL top and bottom simultaneously, and identify horizontal heat advection as a main driver aiding solar surface heating in this midrange mountain valley. We conclude that heterogeneous land use and mountainous topography cause complex interactions between valley-scale and local airflows leading to thermal signatures characterized by strong, small-scale variability. Our study highlights DTS as a crucial tool for investigating complex thermodynamic processes.

Plain Language Summary On calm nights, a nocturnal stable boundary layer forms near the Earth's surface characterized by increasing temperatures with height and very little mixing. Its counterpart is the daytime convective boundary layer, CBL, which has the opposite characteristics. Both the stable and convective boundary layers have received much attention; however, the in-between morning transition (MT) has received less attention, which can degrade weather and air quality forecasts. To better understand the morning transition, we measured air temperature below a tethered balloon and on a tower during the MT with a technique called distributed temperature sensing (DTS) using thin fiber-optic cables. Our unique design enabled an unprecedented view of the MT revealing its detailed and fast-changing structure. The morning transition is a highly variable process whose theoretical description and experimental investigation had previously been simplified due to observational limitations. We found that it starts simultaneously at the top and bottom of the stable layer, and can take an hour to complete. It is strongly influenced by the surrounding land. While more work using DTS is necessary to understand why the air takes so long to respond to the rising sun, we demonstrate how critical this technique is for future research.

1. Introduction

The midlatitude atmospheric boundary layer, ABL, undergoes a diurnal cycle between a daytime convective boundary layer, CBL, and a nocturnal stable boundary layer, SBL when strong synoptic forcing is absent (Stull, 1988). The morning transition (MT) is of interest for weather and air quality forecast as it impacts the distribution of temperature, humidity, and pollutants in the developing CBL (e.g., Holtslag et al., 2013; Morbidelli et al., 2011). Nevertheless, it is difficult to investigate and understand since important drivers including advection, shear, and entrainment are typically simplified or neglected (Angevine et al., 2020; Bange et al., 2007; Wildmann et al., 2015).

Numerous studies investigated the MT using field campaigns and numerical experiments. Angevine et al. (2001) and Svensson et al. (2011) defined the MT by the times between sunrise, the first sign change of sensible heat flux, H , and first statically unstable stratification across 200-m height. Angevine et al. (2001) found that the surface heat flux alone was too weak to drive the transition at the observed speed emphasizing the importance of an entrainment heat flux from above the SBL. Similarly, Lapworth (2006) found a close relationship between sign changes in H and static stability. Further studies found that the entrainment

© 2021. The Authors.

This is an open access article under the terms of the [Creative Commons Attribution License](https://creativecommons.org/licenses/by/4.0/), which permits use, distribution and reproduction in any medium, provided the original work is properly cited.

from the residual layer into the SBL is shear driven (Beare, 2008) and that longwave radiative cooling in the SBL and the residual layer enhance the growth rate of the CBL (Edwards et al., 2014; Wildmann et al., 2015).

Previous studies mainly focused on flat terrain (Angevine et al., 2001; Basu et al., 2008; Higgins et al., 2018; Lapworth, 2006; Svensson et al., 2011). They found that surface heterogeneity strongly modifies the diurnal cycle of the ABL and particularly the MT (Angevine et al., 2020; Holtslag et al., 2013; Wildmann et al., 2015). Hence, further studies on heterogeneous and mountainous terrain are needed to broaden our understanding of the MT.

Past experiments were conducted using point observations, remote sensing, and probes underneath a balloon or remotely piloted aircraft. They were limited in vertical resolution and spatial coverage of synchronous measurements, and consequently relied on assumptions including stationarity or negligible heat advection, which are commonly violated during the transition (Wildmann et al., 2015). In contrast, Raman spectra fiber-optic distributed temperature sensing, (DTS) (Selker et al., 2006; Thomas & Selker, 2021; Tyler et al., 2009), can overcome these limitations through continuous observations along a fiber-optic cable at fine spatial (≈ 0.12 – 0.5 m) and temporal (≈ 1 – 10 s) resolutions. It has successfully been used for investigating the near-surface boundary layer (Cheng et al., 2017; Krause et al., 2013; Thomas et al., 2012; Zeeman et al., 2015) and for atmospheric profiling (Higgins et al., 2018; Keller et al., 2011). The latter studies, however, were either limited in maximum flight height (120 and 100 m), duration (30 min and 17 h), spatial (0.25 and 1.0 m), or temporal resolution (20 s and 5 min), respectively. We show here that DTS, when used to its full capabilities, can uniquely observe the finer scales of the MT evolution. While other studies also measured fine-scale turbulent structures of, e.g., ABL clouds (Kumala et al., 2013; Siebert et al., 2021) or SBL structure (Kral et al., 2021), their observations are snapshots without offering fine temporal resolution.

We demonstrate this substantial expansion of DTS-based MT observations on three summer days in 2019. DTS was deployed below a tethered balloon (2–200-m height), along a tower (0.7–10.9 m), and across a horizontal array (150 by 60 m, at 1 m) in a broad, midrange mountain valley in southeast Germany (see Figures S1 and S2). The static stability derived from these spatially continuous synchronous temperature observations gave detailed, novel insights into the MT's thermodynamics. The DTS observations were amended by traditional sonic anemometry and ground-based radio-acoustic remote sensing.

2. Methodology

2.1. Experimental Site

In June and July 2019, the Large eddy Observatory Voitsumra Experiment 2019 (LOVE19) took place in a broad, midrange mountain valley in the Fichtelgebirge mountains, southeast Germany (50.0906N 11.8543E; 624 m asl; Lapo et al., 2020). The valley stretches from southwest to northeast with a main wind direction along the valley in the lowest 300 m, channeled by the surrounding ridges (Figure S1). At the perennial extensive grassland site located in the flat valley bottom, all instruments were deployed with a maximum distance of 300 m of each other (Figure S2). An isolated forest patch of ~ 15 m canopy height was located about 170 m southeast of the site and delayed direct-beam radiation reaching the south of the site during sunrise.

2.2. Observational Systems

2.2.1. Flying Fiber-Optics Experiment (FlyFox)

A fiber-optic cable was attached to a tethered balloon launched to a maximum altitude of 200 m above ground level (agl) observing air traffic safety regulations (Figure S2c). Air temperature was observed using a DTS instrument (XT, Silixa, UK) with a 10 s temporal and 0.254-m spatial resolution using water baths for calibration (supporting information S2). Immediately below the balloon, a tethersonde was deployed to observe barometric pressure, air temperature, and relative humidity at 1-s intervals (BME280, Bosch sensor tec GmbH, Germany). While nonlinear approaches were tested, linearly approximating the height of each measurement along the fiber-optic cable between the surface and the balloon's flight altitude yielded sufficiently accurate results (supporting information S3).

2.2.2. DTS at the Tower (Tower-DTS)

Fiber-optic cables were deployed along a tower between 0.7- and 10.9-m height (Figure S2b) and air temperature was sensed with a DTS instrument (Ultima, Silixa, UK) with 1 s and 0.127 m sampling resolution using solid-state reference baths (supporting information S2). In postprocessing, data were further aggregated to 10 s averages to reduce the influence of instrument noise.

2.2.3. Sonic Anemometers

Four sonic anemometers (CSAT3, Campbell Scientific, USA) were mounted on the tower at heights of 0.5, 1.25, 4, and 12 m (Figure S2b, supporting information S1). In contrast to common choices (30 min) for energy balance studies, turbulent fluxes were computed using the eddy-covariance technique at a perturbation and averaging time scale of 1 min to correctly capture the transport by the short-lived turbulent eddies during the highly in stationary MT.

2.2.4. Sodar-Rass

The radio-acoustic profiler (Model DSDPA90.64 and 1.29 GHz RASS, Metek, Germany) measured wind speed, wind direction, and potential temperature averaged over 10 min at 20 m gate spacing between 30-m and 300-m height about 90 m northeast of the tower (Figure S2a).

2.2.5. Ancillary Observations

A horizontal fiber-optic array was constructed from the same PVC-jacketed cable used for FlyFox in a rectangular geometry (150 × 60 m) at ~1-m height around the tower. Air temperature was observed following the same procedure as the Tower-DTS and FlyFox (Figure S2a). The array was used to quantify the horizontal temperature perturbations, gradients, and sensible heat advection in combination with sonic wind speeds at 1.25 m following Moderow et al. (2007). Net and solar radiation were observed at 2 m height by a 4-component radiometer (aspirated CNR-4, Kipp&Zonen, Netherlands) at the weather station (Figure S2a). A ceilometer (CHM 8k, Lufft, Germany) located ~300 m northeast of the tower measured cloud cover and cloud base heights at a 1-min temporal and 5-m spatial resolution.

2.3. Computing Static Stability

From FlyFox and Tower-DTS measurements, potential temperature, θ , was computed and static stability was estimated using approximate finite differencing from

$$\frac{\Delta\theta}{\Delta z}(z) = \frac{\langle\theta[z, z + \Delta z]\rangle - \langle\theta[z - \Delta z, z]\rangle}{\Delta z}, \quad (1)$$

where $\langle \rangle$ indicates spatial averaging along the vertical coordinate. The approximated vertical gradients were derived continuously across the profiles using rolling block averages with a window size of $\Delta z = 1.3$ m and $\Delta z = 4.0$ m for the Tower-DTS and FlyFox, respectively. Different calculation methods and window sizes were tested, but the reported choices had a desired trade-off between sharpness of gradients and reducing the effects of measurement uncertainty. Static stability was used to derive layers with a system-specific minimum lifetime (see supporting information S4) and classified as stable ($\frac{\Delta\theta}{\Delta z} \geq 0.04$ K/m) or nonstable ($\frac{\Delta\theta}{\Delta z} < 0.04$ K/m) to best capture the change from SBL to CBL. While this threshold appears far from neutral or convective, we chose a most conservative estimate to delineate the SBL (supporting information S4). Smaller thresholds yielded discontinuous layers, aggravating determination of the MT onset due to the highly instationary nature of the MT by definition, which is an interesting result in itself (see Section 4).

For potential temperatures from sonic anemometers and Sodar-Rass, temperature gradients were calculated between adjoining instruments or gates, respectively. Prior to differencing, instrument-specific biases in absolute sonic temperatures were found to be < 0.2 K.

2.4. Defining the Morning Transition Phase

Consistent with previous studies, we use the terminology MT to refer to the general process of the transition from SBL to CBL. However, we additionally define the MT phase (MTP) as the period between its onset, determined from the first appearance of nonstable conditions to its end, determined by the complete disappearance of the SBL. This novel definition is motivated by the unique, fine-scale spatiotemporal tracking of the DTS technique. Details on the SBL definition are explained in supporting information S4.

For Tower-DTS and FlyFox, the MTP onset may occur separately for the SBL bottom and the top. We chose the earliest time. The bottom-start occurs with the first appearance of nonstable conditions, while the top-start for FlyFox was derived from a segmented linear regression of its upper boundary. The breakpoint of the segmented regressions was varied in time and height, and we selected the optimal regression with the largest mean R^2 for both linear models. The breakpoint of the optimal model signifies the trend change of the SBL top and thus the MTP onset. The slope of the linear model after MTP onset readily quantifies the entrainment velocity.

For the Sodar-Rass, the MTP starts when the SBL height permanently falls below its mean nocturnal height computed between midnight and 05:00 (UTC). For the sonic profiles, two alternative point-based definitions of MTP onset were tested: the first change of sign in H from negative to positive, and from stable to nonstable static stability at any level (supporting information S1).

3. Results

All three mornings were characterized by weak winds (≤ 2 m/s) within the lowest 150 m and a high relative humidity before sunrise ($\geq 90\%$), but no precipitation or fog. Winds above the SBL were predominantly easterly along the valley axis while within they varied between southerly (Figures 1 and 2 for MT1 and MT2, respectively) and northerly (Figure 3, MT3). Near the surface, wind directions showed strong variability across the three MTs (Figures 1–3e). All days had heat advection variable in both sign and magnitude toward the measurement tower at 1-m height before the MTP start, but then consistently switched to positive advection during the MTP (Figures 1–3f). Before its start, intense but small-scale heterogeneity was observed on all days, indicative of submesoscale motions (Pfister et al., 2019). A time delay of about 40 min was observed between the downwelling shortwave radiation exceeding 40 W/m^2 at the net radiometer near the tower and the direct-beam solar radiation reaching the FlyFox launch site due to shading from a nearby forest (Figure S2). The horizontal DTS array showed strong heterogeneity in temperatures, with differences of up to $3.1 \text{ K} \pm 0.32 \text{ K}$ (Figures 1–3f). With MTP onset, the submesoscale thermal structures disappeared, giving way to a larger-scale horizontal temperature gradient across the field, with colder air near the FlyFox launch site and warmer air to the north, especially on sunnier days (MT2, MT3) likely caused by gentle, but persistent cold-air valley-slope flows acting in concert with the residual cold-air pool. When MTP ended, the larger-scale horizontal thermal structures were replaced by their smaller-scale CBL counterparts.

3.1. MT1

The morning of July 22, 2019 had cloud cover between $\frac{2}{8}$ and $\frac{5}{8}$ at ~ 7.5 km. Shortly before the flight, surface winds meandered at all levels until 03:20. Until 04:40 wind directions were mostly stationary at 12 m, but characterized by smaller-amplitude meandering at lower heights with a mean directional change of $39^\circ \pm 20^\circ$. After 05:45, strong directional changes typical of the CBL started to dominate.

Near the surface, the sonic profile revealed that stability changed before sign crossover in H with a delay of about 22 min (Figure 1d). In fact, stability change across all levels was completed shortly before the first change of sign of H at 1.25 m. The sonic MTPs lasted 20 and 51 min for stability and fluxes, respectively. The Tower-DTS MTP started even earlier at 04:08 slightly aloft between 3.2 and 6.0 m (Figure 1c, first black contours) and co-occurred with solar radiation exceeding 40 W/m^2 . Below this height, the stratification remained stable for an additional 15 min. Between its onset (04:08) and its end (04:42, 34-min duration), the SBL contained pockets of neutral or unstable air illustrated by closed, but disconnected SBL contours (Figure 1c).

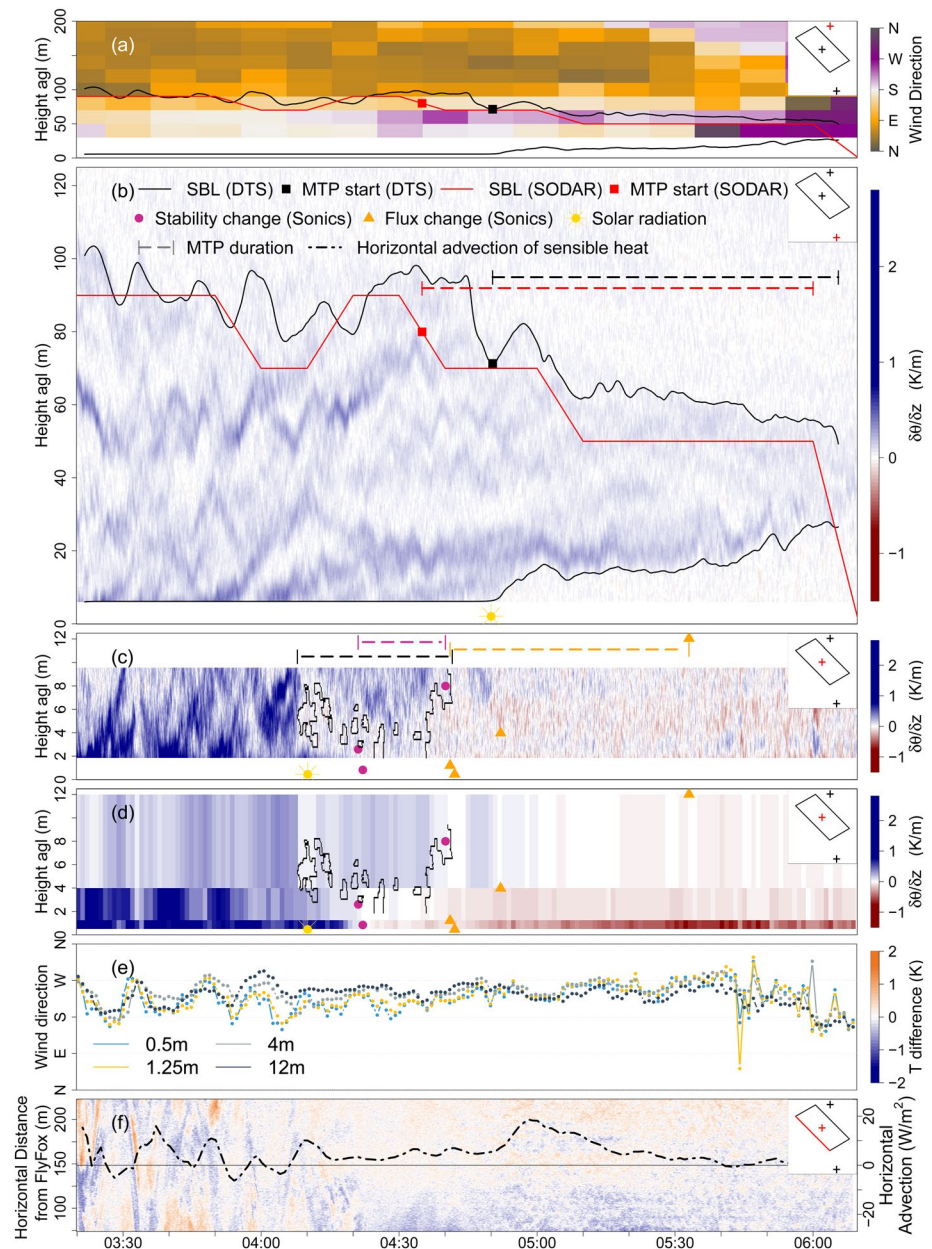


Figure 1. Observations for MT1 (July 22, 2019). (a) Wind directions measured from Sodar-Rass at height above ground level (agl); (b) potential temperature gradients from FlyFox; (c) Potential temperature gradients from Tower-DTS; (d) potential temperature gradients from sonic anemometers; (e) sonic anemometer wind directions; (f) colors represent the horizontal temperature perturbations from its spatial mean along the western border of the DTS array on a color scale shown on the right of panel (e) for illustrational purposes, and the dashed-dotted line quantifies the heat advection across the horizontal DTS array over the lowest 1 m. In panels (c and d), the transition from stably stable to nonstable stratification (dots) and negative to positive sensible heat flux (triangles) is marked (see Section 2.4 and supporting information S1). The small insert in panels (a–d and f) marks the location of the observational system (red) in relation to the field layout (compare Figure S2). See legend in panel (b) for explanation of symbols; sun symbol marks time when solar radiation exceeded 40 W/m^2 . DTS, distributed temperature sensing.

In FlyFox and Sodar-Rass observations, the MTP lasted 76 and 85 min, respectively, with an earlier onset in Sodar-Rass compared to FlyFox (15 min), but a similar end time (Figures 1a and 1b). The effective entrainment velocity (see Section 4.2 for definition) computed from FlyFox data was -0.0068 m/s with a wind directional change of $58^\circ \pm 24^\circ$ at the SBL top. FlyFox MTP onset coincided at the top and bottom with the arrival of direct solar radiation at the launch site. The rate of elevational change of the upper and lower

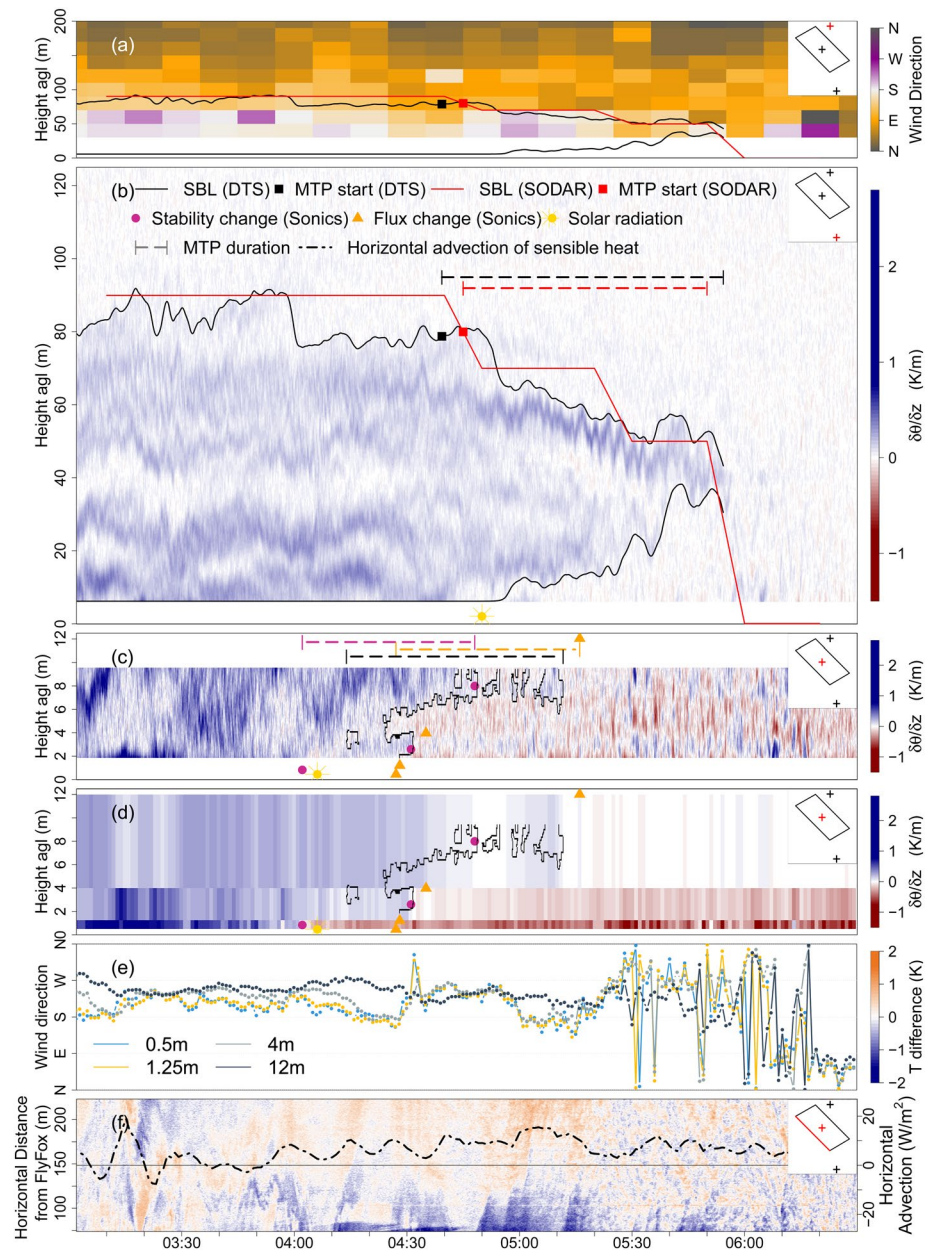


Figure 2. As in Figure 1 but for MT2 (July 23, 2019).

SBL boundary was similar. Compared to the other days, the CBL growth from below was remarkably slow (compare Figures 2 and 3b).

3.2. MT2

On July 23, 2019, cloud cover was least with a maximum of $\frac{1}{8}$ at ~ 10 km, accentuating the influence of the nearby forest patch casting shade on the ground, preserving the cold-air pool and causing stark horizontal temperature perturbations (Figure 2f). From start until 05:25, surface wind directions were mostly stationary at 12 m, but showed consistent small-amplitude meandering below. After 05:25 strong directional changes typical for the CBL occurred. While the durations of the sonic profile MTPs

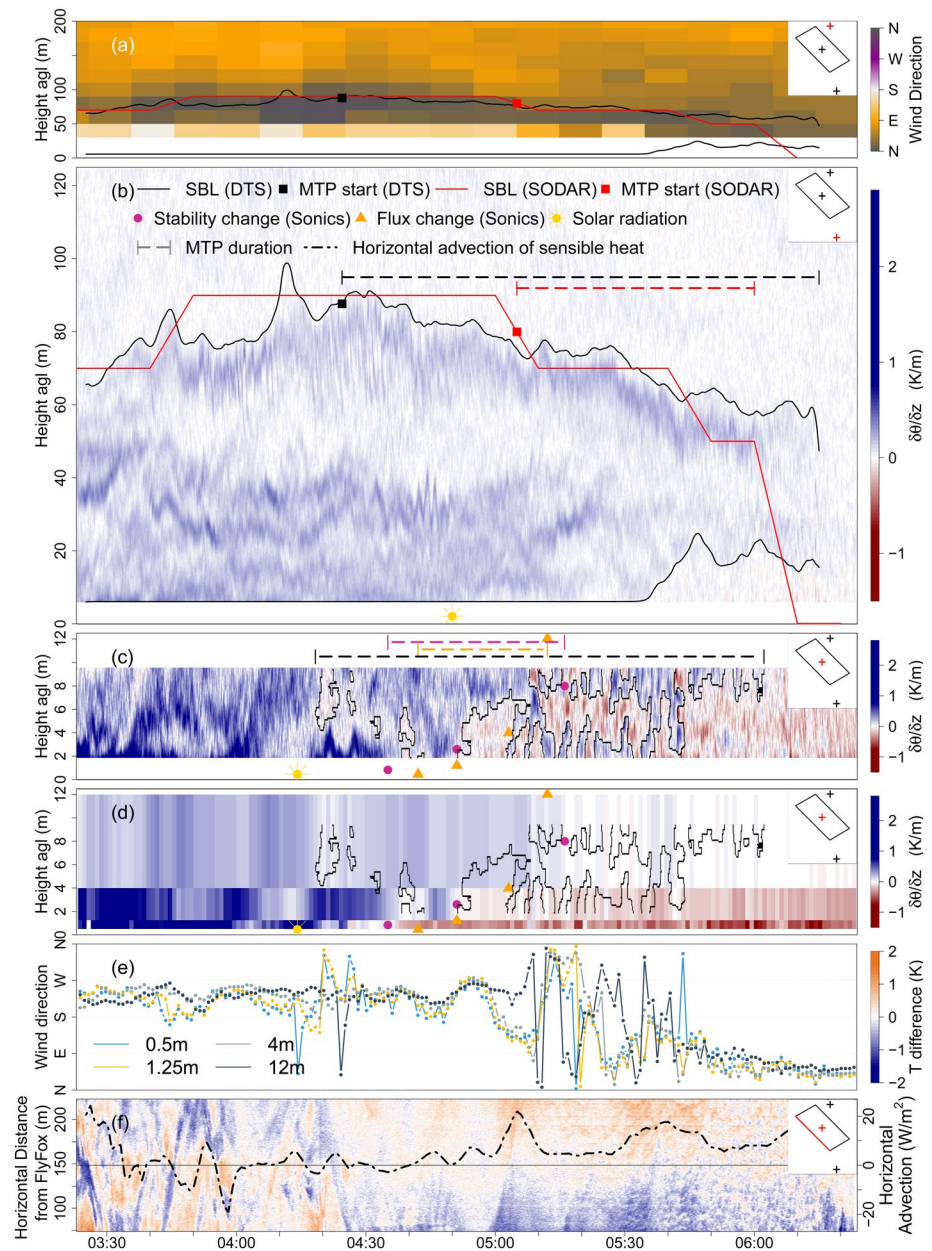


Figure 3. As in Figure 1 but for MT3 (July 26, 2019).

from stability and H change were similar (46 and 49 min, respectively), the first preceded the latter by 25 min (Figure 2d). Unlike MT1, the onset started at the lowermost level. For Tower-DTS, MTP commenced on 04:14 between 3.2 and 4.5 m, pausing for about 10 min, and then continuing until 05:12, lasting a total of 58 min (Figure 2c). The MTP onset from Tower-DTS occurred between the onsets from the sonics.

FlyFox revealed an MTP duration of 75 min and an effective entrainment velocity of -0.0072 m/s with a wind directional change of $40^\circ \pm 32^\circ$ at the SBL top (Figure 2a). The MTP onset occurred at the top (04:39), followed by the transition at the bottom (4:54), which started shortly after the sun reaching the launch site (Figure 2b). MTP onset from Sodar-Rass co-occurred with that from FlyFox within 5 min and lasted 65 min.

3.3. MT3

On July 26, 2019, cloud cover was intermediate between $\frac{2}{8}$ and $\frac{7}{8}$ at ~ 7 km. Near the surface, winds across all levels meandered with increased amplitudes below 4 m until 05:00. Between 05:00 and 05:45, winds were exceptionally calm (< 0.6 m/s) accompanied by rapid asynchronous wind directional changes between the top and lower levels (Figure 3e). After 05:45, wind speeds increased rapidly and turned to northeast. The stability change in sonic profile observations led the MTP onset compared to the sign change in H by 7 min, starting at the lowest level for both, but completed 4 min later, which resulted in a 11 min difference in duration (41 and 30 min, respectively). In contrast, the Tower-DTS detected the greatest MTP duration of all cases, persisting over 104 min. It started with the earliest onset of all observational systems at 04:18, pausing multiple times for several minutes, and then grew fast from 04:51 on, but revealing strong stability and temperature changes (Figure 3c).

Similar to the Tower-DTS, FlyFox revealed its longest MTP duration at 111 min resulting in a relatively small effective entrainment velocity of -0.0049 m/s. The wind directional change at the SBL top was smallest of all cases ($21^\circ \pm 12^\circ$). In contrast to the other cases, the FlyFox MTP onset at the SBL top preceded the transition at the bottom by 68 min, and occurred 40 min earlier than MTP onset in Sodar-Rass observations. The bottom transition change for FlyFox occurred ~ 30 min after the direct-beam solar radiation reached the launching site, resulting in a remarkably long delay.

4. Discussion

4.1. Comparing MTPs Across Observational Systems

The sonic profile observations yielded significant differences in both timing and duration between stability and flux-based approaches. The onset in stability preceded that in fluxes consistently for all cases. These periods of counter-gradient fluxes varied in duration between 25 min (MT2) and 7 min (MT3). The latter finding is sensitive to our choice of the stability threshold (0.04 K/m), and depends on the different height and layer representations between approaches. The flux change is calculated at each instrument height, while stability change is calculated at the mid-interval between two adjacent levels. To eliminate ambiguity in MTP onset, we propose to define the MTP solely from the change in static stability consistently across observational systems for ease of comparison, since this parameter can be derived for more sensors including the DTS technique.

For the stability-based approaches near the surface, the sonic and Tower-DTS observations showed large, height-dependent deviations up to +17 min (MT3) for the 0.5 and 1.25 m sonics and +33 min (MT3) between 1.25 and 4 m sonics. The height intervals across systems were uneven at Δz of 0.75, 2.75, and 8 m for the sonic profile, while Δz was fixed at 1.3 m for the Tower-DTS. Except for MT2, the Tower-DTS transition commenced earlier since it captured short-lived, spatiotemporally confined, nonstable structures evident as closed contours, which were left undetected by the relatively crude sonic profile. The latter missed the rapid and fine-scaled signatures of warmer air evident from Tower-DTS, particularly for MT3, for which they continued for 59 min after the sonic MTP end. Note that the richness in structure from Tower-DTS data stems from the spatial thermodynamical heterogeneity of the near-surface air, which appears as strong temporal variations when advected past the high-resolution 1-D profile.

Only FlyFox detected a lowering of the SBL top simultaneously with its rising bottom. The Sodar-Rass missed the bottom dynamics due to its coarse vertical resolution and elevated lowest gate, rendering it unable to resolve temperature gradients below 50 m agl. Comparing FlyFox and Sodar-Rass observations, the MTP onset and duration agree within 15 min for MT1 and MT2, while they disagreed substantially for MT3. This discrepancy is not surprising as the insufficient resolution of the Sodar-Rass inhibited the detection of the gentle lowering of the SBL top. While the height difference of SBL top at MTP start and end was similar for all cases, the effective entrainment velocity was smallest for MT3 likely due to stronger stability. Winds were calmest that day, which led to less shear-generated mixing and preserved the rich spatial thermodynamic heterogeneity of the near-surface air over 2 h after sunrise. This heterogeneity is likely caused by the mountainous topography creating a variety of competing flows. These may include synoptic flows channeled along the valley and local gravity-driven cold-air currents due to radiative cooling of the valley slopes or the forest canopy.

FlyFox observed a variety of spatiotemporal scales characterizing the MTP and revealed for the first time its entire evolution over hours. Note that our 1-D Tower-DTS and FlyFox DTS still require assumptions about cross-wind flow and spatial structure, which can be circumvented by quasi 2-D and 3-D array geometries (Thomas et al., 2012; Zeeman et al., 2015). However, we can directly quantify the inherent instationary thermal structure, which revealed that the MTP is a much more complex process than a simple 1-D evolution of the CBL eroding the SBL. It can start over several meters simultaneously (Figure 2c) or independently at different heights separated by interspersed stable layers interrupting the growth of the CBL (Figures 1 and 3c). While these results may be caused by the mountainous topography interacting with heterogeneous land use, the complexity makes differentiating between SBL and CBL nontrivial during the MTP. This important finding has been obstructed by traditional point or lower-resolution profile observations, emphasizing the need for methods with fine spatiotemporal resolution such as DTS.

4.2. Factors Controlling SBL Depth

The influence of the surrounding mountains was also reflected in the depth of the SBL, which averaged 90 m in both FlyFox and Sodar-Rass observations and was thus deeper compared to studies in flat terrain (Higgins et al., 2018; Keller et al., 2011). Our observational depth was supported by Large Eddy Simulations for LOVE19 (not shown). FlyFox provided the first direct observational evidence and quantification of the effective entrainment velocity from the SBL top during MTP, confirming the proposed mechanism concluded in previous experiments but lacking direct measurements (Angevine et al., 2001; Lapworth, 2006). Note that our approach cannot separate between true entrainment and height changes of the SBL top from advection, we therefore use the terminology “effective”. We exclude wind speed shear as a plausible physical mechanism causing entrainment during MTP, at least at this site, which had been indirectly concluded before (Angevine et al., 2001; Beare, 2008; Lapworth, 2006). From Sodar-Rass, we demonstrated that wind speed shear was small $\left(0.05 \frac{1}{s}\right)$ in all cases and did not change with MTP onset. However, all cases showed significant directional shear at the SBL top (Figures 1–3a). MT3 had the slowest effective entrainment velocity and a substantial directional variability across the SBL compared to MT1 and MT2. We attribute these findings to the weaker topographic channeling of the valley flow in the lowest hundreds of meters in response to weaker synoptic forcing, resulting in weaker directional shear at the SBL top and a slower MT.

4.3. Factors Controlling SBL Bottom Transition

Despite their observational overlap close to the ground (~ 4 m), FlyFox and Tower-DTS observations revealed spatial differences in MTP dynamics at their separation distance (~ 160 m). The horizontal DTS observations (Figures 1 and 3f) revealed that this substantial horizontal thermodynamic heterogeneity resulted from topography-driven airflows and the influence of shading during sunrise. The heterogeneity generated substantial horizontal heat advection of the same magnitude (Figures 1 and 3f) as the sensible heat fluxes (not shown). Shortly before MTP onset for MT1, the lower two sonic anemometers observed southerly winds while the upper two measured westerly flows (03:50–04:30, Figure 1e). The horizontal DTS revealed colder air in the southern compared to the northwestern part of the array, confirming the existence of local valley-slope flows interacting with the remnant cold-air pool protected by local shading near the FlyFox launch site. The Tower-DTS MTP onset commenced much earlier since it was subject to a positive heat advection directly quantified from the horizontal DTS observations, and the earlier arrival of direct-beam solar radiation. The difference is therefore a combined effect of topographic position and land-use induced shading. Similarly, the competing airflows with contrasting thermal properties may have caused the rapid wind directional changes particularly pronounced at 12 m, coinciding with rapid stability changes and stark horizontal temperature gradients for MT3 (05:00–05:50). The impact of horizontal heterogeneity and advection was considered previously (Angevine et al., 2020; Bange et al., 2007) but it could not be observed directly or was even intentionally eliminated (Angevine et al., 2001, 2020). Our unique DTS observations provide direct evidence that spatially explicit observations help physical understanding of the MT processes and forcings. The impressive detailedness of the SBL structure from FlyFox, Tower-DTS, and horizontal DTS is unparalleled and represents a substantial observational advance.

5. Conclusions

The fine-grained morning transition from the nocturnal SBL to the daytime CBL was observed by employing fiber-optic DTS below a tethered balloon, along a surface tower, and across a horizontal surface array, and compared to that from traditional sonic anemometer and Sodar-Rass sensors. We conclude that the transition dynamics are best derived from spatially continuous observations of static stability, as this quantity offers consistency across observational systems and allows for a physics-based detection of the first appearance of the CBL to the complete disappearance of the SBL. Our choice eliminates ambiguities when using alternative approaches found in previous studies.

In all three cases, the morning transition period near the surface started at multiple heights simultaneously, its timing varied substantially within separation distances of few hundreds of meters, and was characterized by counter-gradient heat transport. We explain our findings as the interaction between heterogeneity of nonlocal heat advection, local slope cold-air density currents, cold-air pools, and differential heating of the valley bottom as directly observed by DTS amended by traditional sensors. Our study confirmed that the morning transition occurs simultaneously at the top and bottom of the SBL. Our first quantification of effective entrainment velocities at the SBL top from DTS points at the importance of wind directional shear caused by the interaction of the synoptic flow and the mountainous topography, and is therefore likely site-specific. Our work demonstrates the substantial improvements in understanding and quantifying the morning transition from the DTS observations, making it a key technology for future studies.

Data Availability Statement

All data used in this manuscript can be accessed at <https://doi.org/10.5281/ZENODO.4312976> (Lapo et al., 2020).

Acknowledgments

This project was funded by the European Research Council (ERC) under the European Union's Horizon 2020 research and innovation program (Grant Agreement 724629 DarkMix), and the Oberfrankenstiftung.

References

- Angevine, W. M., Baltink, H. K., & Bosveld, F. C. (2001). Observations of the morning transition of the convective boundary layer. *Boundary-Layer Meteorology*, *101*(2), 209–227. <https://doi.org/10.1023/A:1019264716195>
- Angevine, W. M., Edwards, J. M., Lothon, M., LeMone, M. A., & Osborne, S. R. (2020). Transition periods in the diurnally-varying atmospheric boundary layer over land. *Boundary-Layer Meteorology*, *177*, 205–223. <https://doi.org/10.1007/s10546-020-00515-y>
- Bange, J., Spieß, T., & van den Kroonenberg, A. (2007). Characteristics of the early-morning shallow convective boundary layer from Helipod Flights during STINHO-2. *Theoretical and Applied Climatology*, *90*(1–2), 113–126. <https://doi.org/10.1007/s00704-006-0272-2>
- Basu, S., Vinuesa, J.-F., & Swift, A. (2008). Dynamic LES modeling of a diurnal cycle. *Journal of Applied Meteorology and Climatology*, *47*(4), 1156–1174. <https://doi.org/10.1175/2007JAMC1677.1>
- Beare, R. J. (2008). The role of shear in the morning transition boundary layer. *Boundary-Layer Meteorology*, *129*(3), 395–410. <https://doi.org/10.1007/s10546-008-9324-8>
- Cheng, Y., Sayde, C., Li, Q., Basara, J., Selker, J., Tanner, E., & Gentine, P. (2017). Failure of Taylor's hypothesis in the atmospheric surface layer and its correction for eddy-covariance measurements. *Geophysical Research Letters*, *44*, 4287–4295. <https://doi.org/10.1002/2017GL073499>
- Edwards, J. M., Basu, S., Bosveld, F. C., & Holtslag, A. A. M. (2014). The impact of radiation on the GABLS3 large-eddy simulation through the night and during the morning transition. *Boundary-Layer Meteorology*, *152*(2), 189–211. <https://doi.org/10.1007/s10546-013-9895-x>
- Higgins, C. W., Wing, M. G., Kelley, J., Sayde, C., Burnett, J., & Holmes, H. A. (2018). A high resolution measurement of the morning ABL transition using distributed temperature sensing and an unmanned aircraft system. *Environmental Fluid Mechanics*, *18*(3), 683–693. <https://doi.org/10.1007/s10652-017-9569-1>
- Holtslag, A. A. M., Svensson, G., Baas, P., Basu, S., Beare, B., Beljaars, A. C. M., et al. (2013). Stable atmospheric boundary layers and diurnal cycles: Challenges for weather and climate models. *Bulletin of the American Meteorological Society*, *94*(11), 1691–1706. <https://doi.org/10.1175/BAMS-D-11-00187.1>
- Keller, C. A., Huwald, H., Vollmer, M. K., Wenger, A., Hill, M., Parlange, M. B., & Reimann, S. (2011). Fiber optic distributed temperature sensing for the determination of the nocturnal atmospheric boundary layer height. *Atmospheric Measurement Techniques*, *4*(2), 143–149. <https://doi.org/10.5194/amt-4-143-2011>
- Kral, S., Reuder, J., Vihma, T., Suomi, I., Haualand, K., Urbancic, G., et al. (2021). The innovative strategies for observations in the arctic atmospheric boundary layer project (ISOBAR): Unique finescale observations under stable and very stable conditions. *Bulletin of the American Meteorological Society*, *102*(2), E218–E243. <https://doi.org/10.1175/BAMS-D-19-0212.1>
- Krause, S., Taylor, S. L., Weatherill, J., Haffenden, A., Levy, A., Cassidy, N. J., & Thomas, P. A. (2013). Fibre-optic distributed temperature sensing for characterizing the impacts of vegetation coverage on thermal patterns in woodlands. *Ecology*, *6*(5), 754–764. <https://doi.org/10.1002/eco.1296>
- Kumala, W., Haman, K. E., Kopec, M. K., Khelif, D., & Malinowski, S. P. (2013). Modified ultrafast thermometer UFT-M and temperature measurements during Physics of Stratocumulus Top (POST). *Atmospheric Measurement Techniques*, *6*(8), 2043–2054. <https://doi.org/10.5194/amt-6-2043-2013>
- Lapo, K., Freundorfer, A., Fritz, A., Schneider, J., Olesch, J., Babel, W., & Thomas, C. K. (2020). *Large-eddy Observatory, Voitsumra Experiment 2019 (LOVE19)*. Zenodo, <https://doi.org/10.5281/ZENODO.4312976>

- Lapworth, A. (2006). The morning transition of the nocturnal boundary layer. *Boundary-Layer Meteorology*, *119*(3), 501–526. <https://doi.org/10.1007/s10546-005-9046-0>
- Moderow, U., Feigenwinter, C., & Bernhofer, C. (2007). Estimating the components of the sensible heat budget of a tall forest canopy in complex terrain. *Boundary-Layer Meteorology*, *123*(1), 99–120. <https://doi.org/10.1007/s10546-006-9136-7>
- Morbidelli, R., Corradini, C., Saltalippi, C., & Flammini, A. (2011). Atmospheric stability and meteorological scenarios as inputs to air pollution transport modeling. *Water, Air, and Soil Pollution*, *218*(1–4), 275–281. <https://doi.org/10.1007/s11270-010-0640-5>
- Pfister, L., Lapo, K., Sayde, C., Selker, J., Mahrt, L., & Thomas, C. K. (2019). Classifying the nocturnal atmospheric boundary layer into temperature and flow regimes. *Quarterly Journal of the Royal Meteorological Society*, *145*(721), 1515–1534. <https://doi.org/10.1002/qj.3508>
- Selker, J., van de Giesen, N., Westhoff, M., Luxemburg, W., & Parlange, M. B. (2006). Fiber optics opens window on stream dynamics. *Geophysical Research Letters*, *33*, L24401. <https://doi.org/10.1029/2006GL027979>
- Siebert, H., Szodry, K.-E., Egerer, U., Wehner, B., Henning, S., Chevalier, K., et al. (2021). Observations of aerosol, cloud, turbulence, and radiation properties at the top of the marine boundary layer over the eastern North Atlantic Ocean. *Bulletin of the American Meteorological Society*, *102*(1), E123–E147. <https://doi.org/10.1175/BAMS-D-19-0191.1>
- Stull, R. B. (1988). *An introduction to boundary layer meteorology*. Dordrecht, Boston, London: Kluwer Acad. Publ.
- Svensson, G., Holtslag, A. A. M., Kumar, V., Mauritsen, T., Steeneveld, G. J., Angevine, W. M., et al. (2011). Evaluation of the diurnal cycle in the atmospheric boundary layer over land as represented by a variety of single-column models: The second GABLS experiment. *Boundary-Layer Meteorology*, *140*(2), 177–206. <https://doi.org/10.1007/s10546-011-9611-7>
- Thomas, C. K., Kennedy, A. M., Selker, J. S., Moretti, A., Schroth, M. H., Smoot, A. R., et al. (2012). High-resolution fibre-optic temperature sensing: A new tool to study the two-dimensional structure of atmospheric surface-layer flow. *Boundary-Layer Meteorology*, *142*, 177–192. <https://doi.org/10.1007/s10546-011-9672-7>
- Thomas, C. K., & Selker, J. S. (2021). Optical fiber-based distributed sensing methods. In T. Foken (Ed.), *Springer handbook of atmospheric measurements* (pp. 609–631). Switzerland: Springer. https://doi.org/10.1007/978-3-030-52171-4_20
- Tyler, S. W., Selker, J. S., Hausner, M. B., Hatch, C. E., Torgersen, T., Thodal, C. E., & Schladow, S. G. (2009). Environmental temperature sensing using Raman spectra DTS fiber-optic methods. *Water Resources Research*, *45*, W00D23. <https://doi.org/10.1029/2008WR007052>
- Wildmann, N., Rau, G. A., & Bange, J. (2015). Observations of the early morning boundary-layer transition with small remotely-piloted aircraft. *Boundary-Layer Meteorology*, *157*(3), 345–373. <https://doi.org/10.1007/s10546-015-0059-z>
- Zeeman, M. J., Selker, J. S., & Thomas, C. K. (2015). Near-surface motion in the nocturnal, stable boundary layer observed with fibre-optic distributed temperature sensing. *Boundary-Layer Meteorology*, *154*, 189–205. <https://doi.org/10.1007/s10546-014-9972-9>